Magnetic order and magnetotransport in half-metallic ferrimagnetic Mn_yRu_xGa thin films

K. E. Siewierska,[1,*] G. Atcheson,[1] A. Jha,[1] K. Esien,[2] R. Smith,[1] S. Lenne,[1] N. Teichert,[1] J. O'Brien,[1] J. M. D. Coey,[1] P. Stamenov,[1] and K. Rode[1]

[1]*School of Physics and CRANN, Trinity College Dublin, Dublin 2, Ireland*

[2]*Queen's University Belfast, Belfast BT7 1NN, United Kingdom*

(Received 8 April 2021; accepted 20 July 2021; published 9 August 2021)

The ruthenium content of half-metallic Mn_2Ru_xGa thin films, with a biaxially strained inverse Heusler structure, controls the ferrimagnetism that determines their magnetic and electronic properties. An extensive study of Mn_yRu_xGa films on MgO (100) substrates with $1.8 \leqslant y \leqslant 2.6$ and $x = 0.5$, 0.7 or 0.9, including crystallographic, magnetic order, magneto-transport, and spin polarization, is undertaken to map specific composition-dependent properties in this versatile ternary system. A comparison of experimental densities obtained from x-ray reflectivity with calculated densities indicates full-site occupancy for all compositions, which implies chemical disorder. All moments lie on a Slater-Pauling plot with slope 1 and all except $x = 0.5$, $y = 2.2$ exhibit magnetic compensation at T_{comp} below 500 K. The coercivity near T_{comp} exceeds 10 T. Increasing the Mn or Ru content raises T_{comp}, but increasing Ru also decreases the spin polarization determined by point contact Andreev reflection. Molecular-field theory is used to model the temperature dependence of the net ferrimagnetic moment and three principal exchange coefficients are deduced. Marked differences in the shape of anomalous Hall and net magnetization hysteresis loops are explained by substantial canting of the small net moment by up to 40° relative to the c axis in zero field, which is a result of slight noncollinearity of the Mn^{4c} sublattice moments due to competing intrasublattice exchange interactions arising from antisite disorder and excess Mn in the unit cell. Consequences are reduced-spin polarization and an enhanced intrinsic contribution to the anomalous Hall effect. The systematic investigation of the physical properties as a function of x and y will guide the selection of compositions to meet the requirements for magnonic and spintronic MRG-based devices.

DOI: 10.1103/PhysRevB.104.064414

I. INTRODUCTION

Zero-moment ferrimagnetic half-metals (ZMHM) are attractive materials for applications in spintronic devices [1,2]. They offer advantages over their antiferromagnetic or half-metallic ferromagnetic counterparts [3]. After their theoretical prediction in 1995 [4], various candidate ZMHM materials were proposed over the years based on DFT calculations, including $C1_b$ CrMnSb, $L2_1$ Fe_2VGa, and $D0_3$ Mn_3Ga [5–7]. Unfortunately, the predicted alloys either crystallized in a different structure with no spin gap like Mn_3Ga [8], or else they decomposed into a mixture of simpler phases like CrMnSb, or were found be either nonmagnetic or very weak ferromagnets, like Fe_2VGa [9]. It seemed there might be some reason why the ZMHM was so elusive [6]. The first material to show evidence of the long-sought magnetic behavior was $Mn_2Ru_{0.5}Ga$ [10]. Extrapolating between a half-Heusler Mn_2Ga and a full-Heusler Mn_2RuGa, $Mn_2Ru_{0.5}Ga$ was thought to have 21 valence electrons with vacancies on half the Ru^{4d} sites, as shown in Fig. 1 [10]. Since its discovery, a few other members of ZMHM material class have been demonstrated, including thin-film Mn_3Al [11] and bulk $Mn_{1.5}V_{0.5}FeAl$ [12]. The Mn_2Ru_xGa (MRG) thin films grown on MgO (001) substrates, where the cubic structure of the inverse Heusler alloy is distorted by biaxial strain, offer perpendicular magnetic anisotropy that allows efficient detection and manipulation of the magnetic state. Cubic MRG would crystallize in the $F\bar{4}3m$ (216) space group, with four formula units (f.u.) per unit cell, which is adopted when referring to crystallographic vectors and positions, but the symmetry is reduced to $I\bar{4}m2$ (119) by the tetragonal distortion. In the ideal inverse XA Heusler structure, 4a and 4b sites are occupied by Mn and Ga, respectively, whereas 4c and 4d sites are fully occupied by Mn and Ru [10]. Transport and magneto-optic properties are dominated by the Mn^{4c} sublattice because there are few, if any, Mn^{4a} states at the Fermi level [1,10,13]. The two manganese sublattice magnetic moments cancel at the compensation temperature T_{comp}. Nevertheless, magnetic domains can be observed by the magneto-optic Kerr effect (MOKE) even at temperatures where there is little or no net magnetization [14,15]. As the net moment tends to zero, the anisotropy field becomes large, resulting in high-frequency spin dynamics with low Gilbert damping [1,10]. A maximum zero-field resonance frequency of ≈160 GHz and a Gilbert damping constant $\alpha \approx 0.02$ have been reported [1,16].

Remarkably efficient charge/spin conversion and large spin-orbit fields per current density $\mu_0 \boldsymbol{H}_{\text{eff}}/\boldsymbol{j}$ related to spin currents have recently been measured in single thin films of MRG, where $\mu_0 \boldsymbol{H}_{\text{eff}}/\boldsymbol{j}$ approaches 0.1×10^{-10} T/Am^{-2} in the low-current density limit. This is almost a thousand times the Ørsted field and one to two orders of magnitude greater

*siewierk@tcd.ie

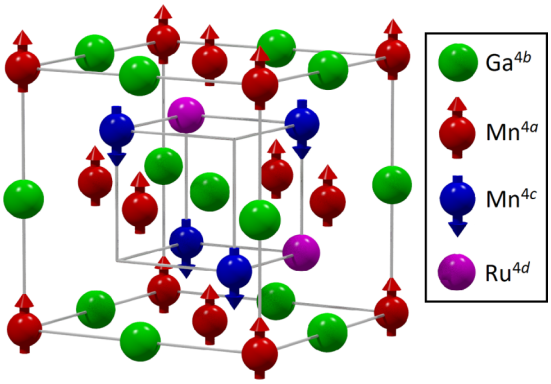

FIG. 1. Model of the inverse Heusler *XA* structure of $Mn_2Ru_{0.5}Ga$.

than $\mu_0 \boldsymbol{H}_{\text{eff}}/\boldsymbol{j}$ in heavy metal/ferromagnet bilayers [17]. The efficiency of current induced spin-orbit torque switching in Ru/MRG/MgO has been found to be similar to that of a ferromagnet, e.g., Ta/CoFeB/MgO [18] or Pt/Co/AlO_x [19], despite larger MRG film thickness and coercivity [20]. Furthermore, thermal single-pulse all-optical toggle switching at ultrashort timescales (<10 ps) has been recently demonstrated in MRG, making it the first non-Gd-based material to exhibit this effect [21–23]. MRG-based devices could offer a practical solution to the current problem of chip-to-chip generation and detection of electromagnetic radiation in the 0.1–10 THz frequency range, known as the "THz gap," provided sufficiently high magnetoresistive effects can be achieved [1,24].

Each spintronic application requires a specific set of material properties. For example, efficient single-pulse all-optical toggle switching at room temperature (RT) in MRG films requires T_{comp} to be just above RT [21]. High-spin polarization and perfectly crystalline films with smooth surfaces are desirable for MRG-based magnetic tunnel junctions. Earlier studies have investigated the variation of some of these properties with x in Mn_2Ru_xGa [10,13,25,26]. The results show that an increase in Ru content increases tetragonal distortion of the cubic unit cell on MgO and improves the wetting of the film. These qualities are useful for all applications and particularly for the fabrication of nanostructured devices [13,25].

The goal of the present work is to help identify compositions that exhibit the best combinations of properties for specific applications. Thin thin films are prepared with varying Ru and Mn content, while keeping the Ga content fixed. The dominant contribution of Mn^{4c} sites to the density of states at the Fermi level allows us to disentangle net and sublattice magnetizations with the aim of establishing noncollinearity of the Mn^{4c} sublattice moments, which results in canting of net moment.

II. METHODOLOGY

Epitaxial thin films of Mn_yRu_xGa (MRG) with $x + y \approx 3$ were grown by DC magnetron sputtering on 10×10 mm^2 (100) MgO substrates in our Shamrock sputtering system [1,10]. The base pressure of the system was 10^{-8} Torr. Films were cosputtered in argon onto single-side polished substrates maintained at 350°C from three 75-mm targets of Mn_2Ga, Ru and either MnGa or Mn_3Ga. Deposition rates from each target were calibrated and used to determine the values of x and y in the formula. Films were capped *in situ* with a 3-nm layer of AlO_x deposited at RT to prevent further oxidation. Film thickness and rms roughness were determined by low-angle x-ray scattering in a Panalytical X'Pert Pro diffractometer, and thickness was found by fitting the interference pattern using X'Pert Reflectivity Software. A Bruker D8 Discovery x-ray diffractometer with a copper tube (K_α wavelength = 154.06 pm) and a double-bounce Ge [220] monochromator on the primary beam was used to determine the diffraction patterns of the thin films. Reciprocal space maps were obtained on the same diffractometer around the (113) MgO reflection.

Magnetization measurements with the field applied perpendicular or parallel to the surface of films mounted in a straw were made using a 5 T Quantum Design SQUID magnetometer. Data included hysteresis loops and thermal scans from 10 to 400 K. They were corrected for the magnetism of the substrate. Thermal scans in zero field after saturation of the magnetization at RT were used to determine the compensation temperatures of the films. For Kerr imaging, an Evico Magnetics wide-field Kerr microscope with a 10×0.25 objective lens was used. All loops were measured with polar sensitivity and red LED light with a field applied out of plane. Faraday rotation was compensated during the measurement using a feature which readjusts the analyzer position relative to a mirror reference [27]. Samples were heated from 300 to 500 K on a temperature-controlled microscope stage.

Electrical measurements were made in a 1 T GMW electromagnet under ambient conditions. Silver wires were cold-welded to the films with indium and the current used was 5 mA. High-field data were obtained in a 14 T Quantum Design Physical Property Measurement System (PPMS). The films there were contacted with silver paint. The 4-point Van der Pauw geometry was used to determine both the Hall resistivity and the longitudinal resistivity of the films.

Point contact Andreev reflection (PCAR) measurements were made in the PPMS using a mechanically sharpened Nb tip. Landing the tip onto the sample surface is controlled by an automated vertical Attocube piezo-stepper. Two horizontal Attocube steppers are used to move the sample laterally to probe a pristine area. The differential conductance spectra were fitted using a modified Blonder-Tinkham-Klapwijk model, as detailed elsewhere [28,29].

III. RESULTS

Typical small-angle x-ray scattering data and fit are shown in Fig. 2(a) and attest to the film quality. Film and cap layer thickness values for all films were 50 ± 5 nm and 3 ± 2 nm, respectively, and root-mean-square roughness was deduced from these data. Figure 2(b) shows simulated XRR patterns with varying MRG layer density only. The minimum and maximum MRG densities are 7700 kg/m^{-3} and 8700 kg/m^{-3}, respectively. A small variation in density produces a large variation in the critical angle and thus shifts the overall pattern. The films are tetragonally elongated by about 1% as a result of biaxial compressive strain imposed by the substrate. A typical x-ray diffraction pattern in Fig. 2(c) shows only the c axis (002) and (004) reflections as expected from a perfectly textured film. The growth axis corresponds to the

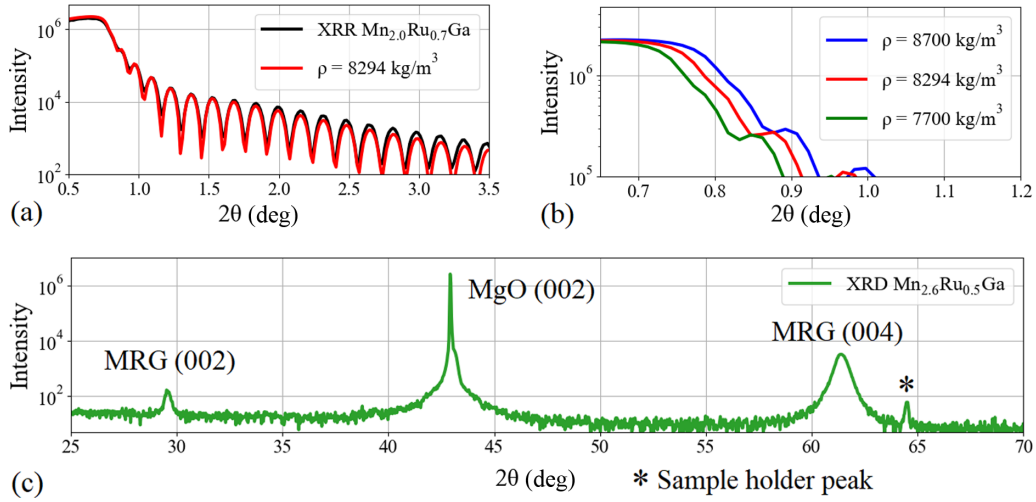

FIG. 2. X-ray analysis of MRG thin films: (a) XRR pattern of $Mn_{2.0}Ru_{0.7}Ga$ with the best fit data, (b) comparison of simulated XRR patterns for various MRG layer densities, and (c) XRD pattern of $Mn_{2.6}Ru_{0.5}Ga$. The peak marked * is due to the sample holder.

crystallographic c axis. Broadening of the reflections is mainly due to the film thickness.

In order to determine both unit cell parameters and to visualize the strain in the film, reciprocal space maps were recorded around the [113] MgO reflection. An example is shown in Fig. 3. The a parameter of MRG is constrained by the substrate to be $\sqrt{2}a_{MgO} = 595$ pm, whereas the c parameter expands by about 1%. The a parameters of the films are shown in Table I, values lie in the range 595 pm $< a <$ 598 pm, which indicates the films are strained. The presence of crystalline defects such as dislocations can be minimized by reducing the film deposition temperature. The defects are seen by Kerr microscopy to act as pinning centers for domain-wall motion [15].

The densities of the films were obtained from the low-angle x-ray reflectivity data. Theoretical densities are calculated from the atomic formulas reduced to exactly four atoms per formula unit using the experimentally determined a and c parameters to determine the cell volume. Calculating densities for $Mn_2Ru_{0.5}Ga$, for example, by assuming full occupancy or two vacancies per unit cell unit gives 7900 kg/m^3 or 7100 kg/m^3, respectively. The density obtained from fitting the XRR pattern was 7800 kg/m^3. This shows that the vacancy assumption underestimates the density by 9%, whereas the experimental density agrees with that calculated for full occupancy to within about 1%. A comparison of experimental and calculated densities of nine films for full occupancy is shown in Fig. 4, where it is seen that the values agree to within 3%. The densities predicted for the formulas with 0.3 or 0.1 vacancies and 0.1 interstitial Mn atoms are marked by yellow crossed bars. We conclude that all the crystallographic sites in MRG really are close to fully occupied. Overall, the density increases with increasing Ru content as expected. The number of valence electrons n_v per f.u. is included in Table I.

Net magnetization and hysteresis were measured by SQUID magnetometry. Compensation temperatures were deduced from the change of sign of the remanent magnetization in zero-applied field found from thermal scans after saturating in 5 T at 400 K. All samples bar one exhibited a compensation point. Some of the thermal scans are presented in Fig. 5. Curie

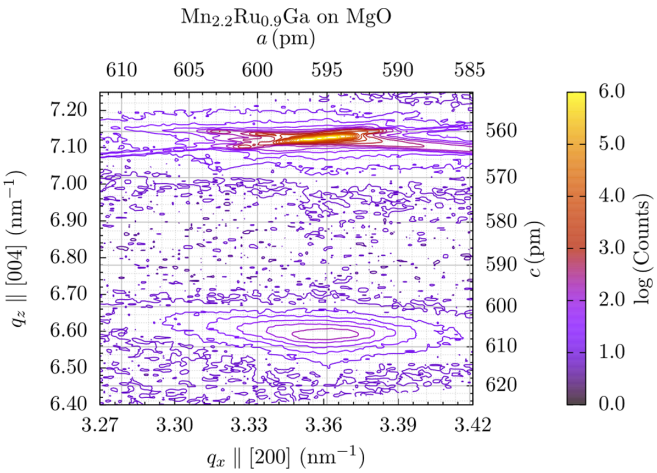

FIG. 3. Reciprocal space map of $Mn_{2.2}Ru_{0.9}Ga$ of MgO (113) and MRG (204) reflections. Lattice parameters are calculated with respect to the MRG unit cell.

TABLE I. Compositions, number of valence electrons, and crystallographic and magnetic properties of three series of MRG thin films where the Mn and Ru content are varied. M_0 and m_0 are magnetization and moment at $T = 4$ K, respectively.

Mn, Ru y, x	n_v	c (pm)	a (pm)	ρ (kg/m^3)	M_0 (kA/m)	m_0 (μ_B/f.u.)	T_{comp} (K)	T_C (K)
2.2, 0.5	24.2	605	597	8003	−33	−0.19	—	550
2.4, 0.5	24.4	604	596	8135	6	0.03	130	577
2.6, 0.5	24.6	604	595	7840	38	0.22	278	592
2.0, 0.7	24.4	605	598	8296	13	0.08	165	530
2.2, 0.7	24.6	605	596	8365	43	0.25	311	543
2.4, 0.7	24.8	606	596	8359	67	0.39	381	494
1.8, 0.9	24.6	608	596	8513	36	0.21	235	478
2.0, 0.9	24.8	606	596	8409	61	0.35	375	513
2.2, 0.9	25.0	607	597	8496	111	0.65	436	491

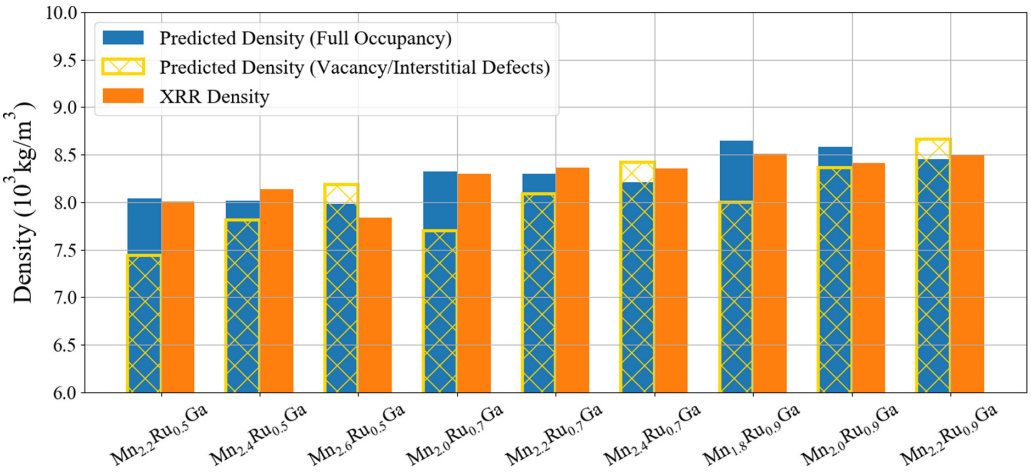

FIG. 4. Calculated (blue) and experimental (orange) densities for the nine MRG films. The yellow crossed bars show densities predicted if there were vacancies/interstitials in the structure.

temperatures were all above 400 K, the temperature limit of our SQUID measurements. Hysteresis in these films can be extremely large close to compensation because the anisotropy field $\mu_0 H_A = 2K_1/M_s$ diverges as the net magnetization M_s falls to zero. The net magnetization measured by SQUID magnetometry with the field applied parallel or perpendicular to the film plane is shown for three $x = 0.5$ films in the top panel of Fig. 6. The coercivity in the out-of-plane loop agrees with that seen in the anomalous Hall effect (bottom panel). All in-plane loops exhibit a soft component that saturates in about 50 mT. This behavior will be discussed in Section V.

The anomalous Hall effect cannot provide the magnitude of the sublattice magnetization as it results from spin-dependent scattering and band-structure effects [30], but the coercivity is determined accurately, and the dominant sublattice is obvious from the loop shape. Figure 7(a) shows the reversal of the Hall loop on crossing compensation. The Hall signal is dominated by the Mn^{4c} sublattice that contributes the majority of states close to the Fermi level. This sublattice is magnetically dominant below, but not above, T_{comp} as can be inferred from the sign of the anomalous Hall coefficient. Sample $Mn_{2.6}Ru_{0.5}Ga$ compensates at 278 K, where the coercivity diverges. The minor loop at RT already exhibits a coercivity of 12 T (Fig. 6, bottom right panel). The anomalous Hall angle at RT, defined as the ratio of the Hall resistivity at saturation to the longitudinal resistivity, reaches a maximum of 2% for the $x = 0.5$ series when $y = 2.2$, as shown in Fig. 7(b). Spin polarization data determined by PCAR are summarized in Fig. 7(c). The $x = 0.5$ series (in black) shows a maximum spin polarization at the Fermi level of 63% for $y = 2.4$. Alloys with a higher ruthenium content have a considerably smaller spin polarization. The spin polarization is linearly dependent on the anomalous Hall angle θ_{AH} for $x = 0.5$ and $y = 2.0, 2.4$ as shown in Figs. 7(d) and 7(e), respectively. This demonstrates that the band structure accounts for θ_{AH}, which is dominated by the lowest concentration of carriers and confirms that Mn^{4c} sublattice electrons dominate the transport. A summary of the crystallographic and magnetic properties on the nine MRG films is provided in Table I. All films show compensation, with the exception of $Mn_{2.2}Ru_{0.5}Ga$.

MOKE signal shown in Fig. 8 is essentially that of the Mn^{4c} sublattice magnetization. The MOKE contrast falls to zero at the ordering temperature, tabulated in Table I. The domain patterns in zero-applied field tend to get frozen by defect networks, or whenever the hysteresis exceeds the stray field due to the small net magnetization [15].

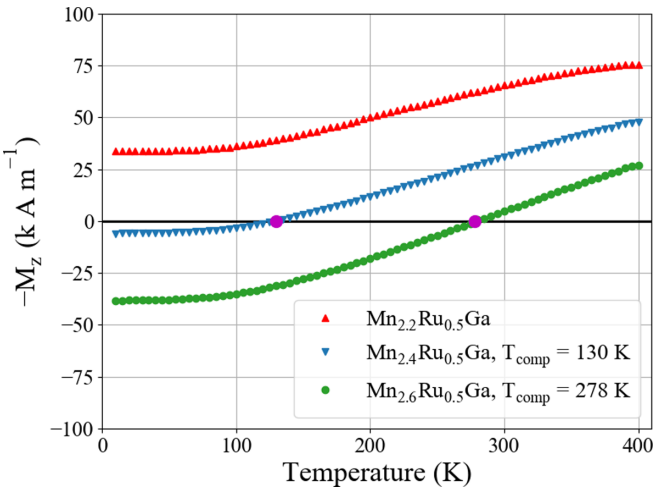

FIG. 5. Temperature scans of the remanence of several MRG films with $x = 0.5$ used to determine the compensation temperature.

IV. MEAN-FIELD THEORY

Zero-field thermal scans of net magnetization measured by the SQUID obtained after saturating the magnetization at 400 K were fitted using a two-sublattice Weiss molecular mean-field model of colinear ferrimagnetism described by the system of nonlinear equations,

$$\begin{aligned} \mathbf{H}^{4a} &= n_W^{aa}\mathbf{M}^{4a} + n_W^{ac}\mathbf{M}^{4c} \\ \mathbf{H}^{4c} &= n_W^{ac}\mathbf{M}^{4a} + n_W^{cc}\mathbf{M}^{4c}, \end{aligned} \tag{1}$$

where H^{4a} and H^{4c} are the internal sublattice molecular fields M^{4a} and M^{4c} are the magnetizations of the two

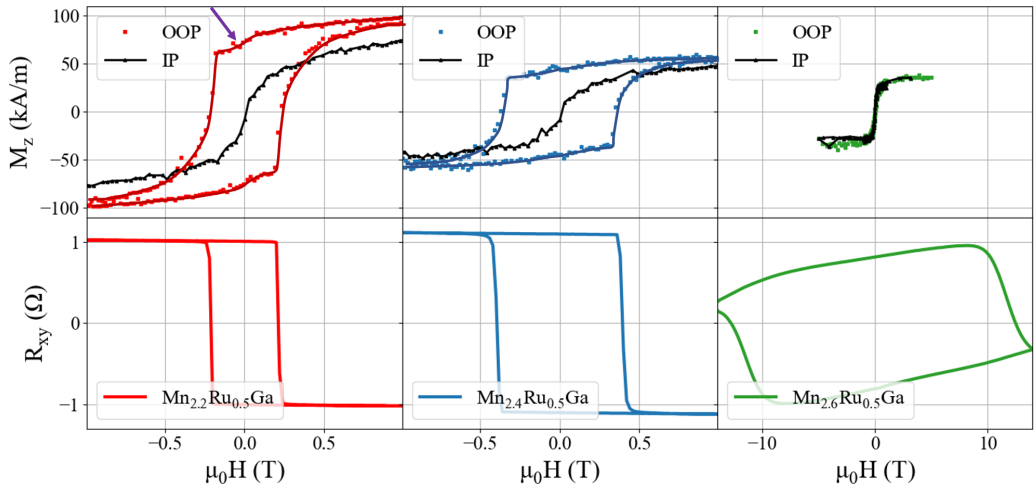

FIG. 6. MRG thin films for the $x = 0.5$ series. Top panel: Magnetization and curves measured parallel (IP) and perpendicular (OOP) to the film plane. Bottom panel: Corresponding anomalous Hall effect curves. Note the applied field in the third panel on the right ranges from −14 T to +14 T.

sublattices, which are modeled by Brillouin functions and n_W^{aa}, n_W^{ac} and n_W^{cc} are the three Weiss coefficients. They are related to Heisenberg exchange constants $\mathscr{J}$ by the expression

$$\mathscr{J}^{ij} = \frac{n_W^{ij}\rho\mu_0(g\mu_B)^2}{Z^{ij}}, \tag{2}$$

where ρ is the number of the Mn atoms on the i-th sublattice per unit cell volume, μ_0 is permeability of free space, g is the Landé g factor for spin, μ_B is the Bohr magneton, and Z is the coordination number, where $Z^{aa} = Z^{cc} = 12$ and $Z^{ac} = 8$ for Mn_2Ru_xGa.

When more than half the sites are occupied by manganese, we assume the excess populates the 4*d* sites that are symmetrically equivalent to the 4*c* sites. The 4*a* and 4*b* sites that accommodate Mn and Ga atoms are assumed to be fully occupied. The spin angular momentum quantum numbers for Mn atoms on each site, $S^{4a,4c}$, are multiples of $\frac{1}{2}$. The upper bound for $S^{4a,4c}$ is the sum of spins in a half-filled 3*d* orbital (5 spins). The lower bound is based on the Mn moment in similar compounds (3 spins), so the quantum numbers in the Brillouin

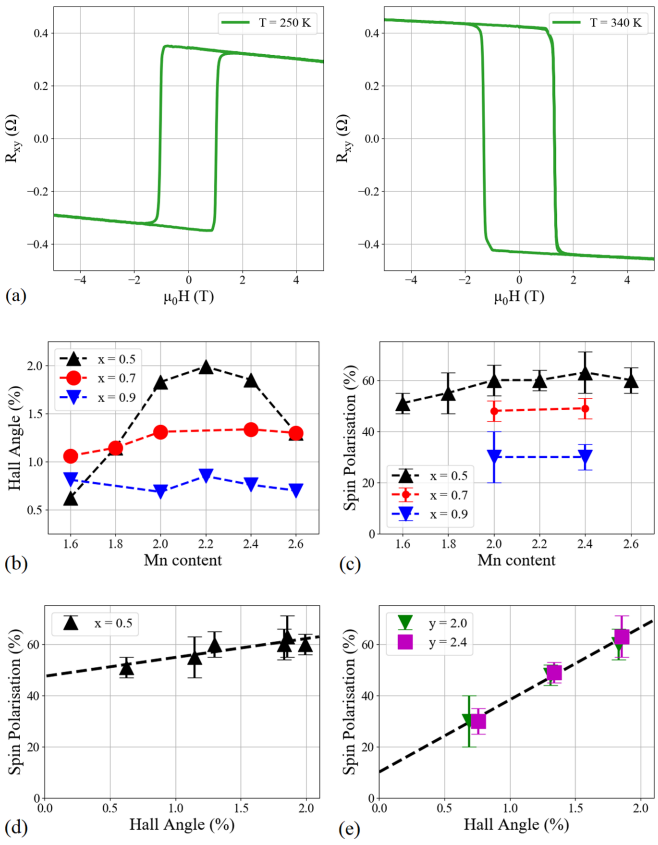

FIG. 7. Anomalous Hall effect: (a) anomalous Hall hysteresis loops for $Mn_{2.6}Ru_{0.5}Ga$ below (250 K), and above (340 K) compensation (T_{comp}= 278 K). (b) Hall angles and (c) spin polarization for three series in an extended range of Mn composition. The spin polarization versus anomalous Hall angle for constant (d) $x = 0.5$ and (e) $y = 2.0, 2.4$.

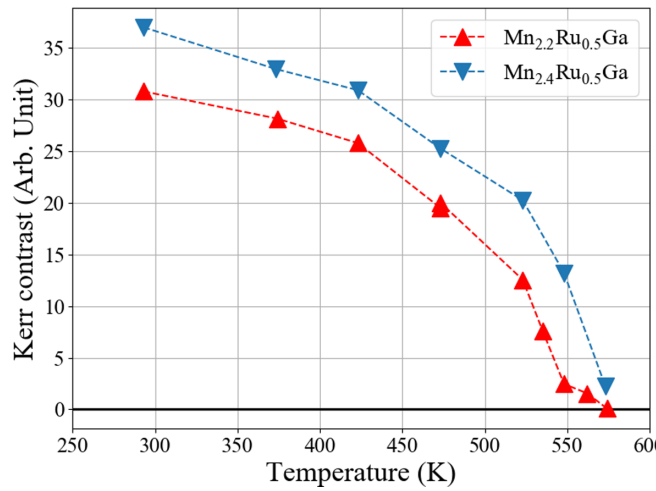

FIG. 8. Temperature dependence of the optically dominant sublattice, measured by MOKE microscopy.

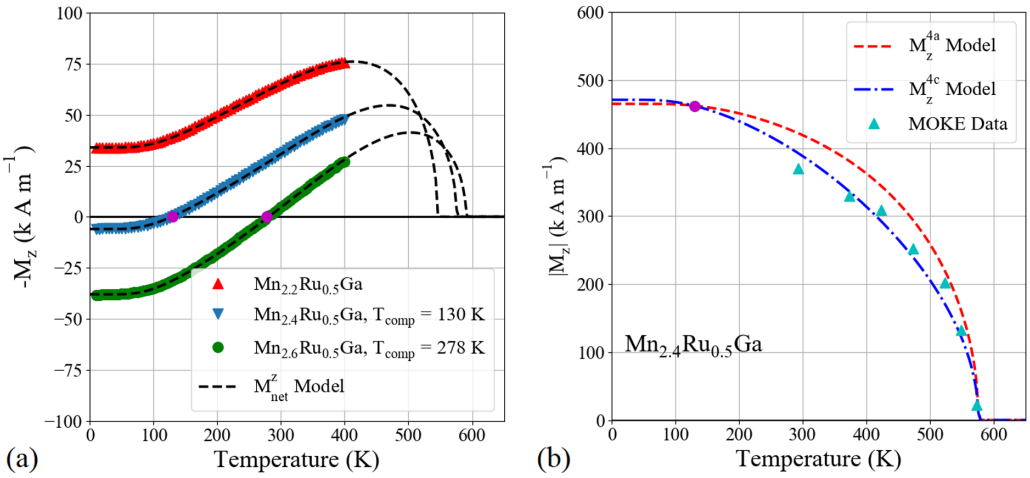

FIG. 9. (a) $Mn_{2.2}Ru_{0.5}Ga$, $Mn_{2.4}Ru_{0.5}Ga$, and $Mn_{2.6}Ru_{0.5}Ga$ thin films: Molecular-field theory fit of net magnetization versus temperature. (b) $Mn_{2.4}Ru_{0.5}Ga$: Calculated temperature dependences of Mn^{4a} and Mn^{4c} sublattice magnetizations compared with scaled MOKE data. The violet point marks compensation.

functions are chosen in the range $1.5 \leqslant S^{4a,4c} \leqslant 2.5$, and the sublattice magnetization is scaled to best represent the data. In metals, the spin moment per atom is rarely an integral number of Bohr magnetons and the sublattice moments at $T = 0\,\mathrm{K}$ cannot be directly calculated from the $S^{4a,4c}$ quantum numbers appropriate for localized electrons due to orbital overlap and mixing. We found by density-functional theory calculation that the Mn^{4a} sublattice moment at $T = 0\,\mathrm{K}$ is nearly independent of Ru content for $0.5 \leqslant x \leqslant 1.0$ with a value of $m_0^{4a} = 2.70\ \mu_B/\mathrm{Mn}$, corresponding to a sublattice magnetization $M_0^{4a} = 465\ \mathrm{kAm^{-1}}$ [25]. The net magnetization at $T = 0\,\mathrm{K}$ was extrapolated from the SQUID magnetometry data, shown in Fig. 5. Using this value, the magnetization of the Mn^{4c} sublattice was inferred.

MOKE microscopy at a fixed wavelength ($\lambda = 632\,\mathrm{nm}$) measures the Kerr rotation, which for MRG is essentially proportional to the magnetization of the Mn^{4c} sublattice. Temperature-dependent MOKE data are compared with M_z of the Mn^{4c} sublattice calculated from the model in Fig. 9(b), validating our approach. We use MOKE to determine T_C, since it covers the appropriate temperature range, and the Curie temperatures are then used as constraints in the fits [31]. The SQUID data, MFT fits, and MOKE data for $x = 0.5$ thin films are all shown in Figs. 9(a) and 9(b).

V. DISCUSSION

We define the Mn^{4c} moment as positive, coupled magnetically to the negative Mn^{4a}. In a previous study it was shown that well below T_C the Mn^{4a} moment is almost temperature independent, whereas the Mn^{4c} moment varies nearly linearly as a function of temperature [26]. Therefore, adding (subtracting) atoms on the Mn^{4c} sublattice is expected to raise (lower) T_{comp}, whereas adding (subtracting) Mn atoms on the Mn^{4a} will increase (decrease) the sublattice moment, but since this moment is negative it results in a decrease (increase) of T_{comp}.

Increasing Ru raises T_{comp}[10] and within each Ru series increasing Mn also increases T_{comp}. Figure 10(a) shows the relationship between T_{comp} and the number of valence electrons (n_v), with a slope of 530 K per electron. We conclude that the added Mn predominantly increases the Mn concentration on the $Mn^{4c/4d}$ sublattice. This is supported by the analysis of the densities of the thin films plotted in Fig. 4, which shows that there is no appreciable vacancy concentration for any composition in the series. Figure 10(b) shows the linear relationship between m_0 and n_v with a slope of 1 μ_B/f.u. per electron. The Slater-Pauling behavior confirms the half-metallicity of all the MRG thin films.

The magnetometry data in Fig. 5 were recorded after magnetically saturating the samples perpendicular to their surface at $T = 400\,\mathrm{K}$. The z projection of the net magnetization was measured in zero field as a function of temperature during cooldown. An ideal data set would include all three components of the sublattice specific moments, which might be obtained using neutron diffraction or, if two components would suffice, by x-ray magnetic circular dichroism (XMCD) [32]. Here we discuss the magnetic mode of MRG first in the simplified model of two collinear sublattices, based on known variations of the Mn-Mn exchange parameters with the distance between interacting atoms.

Table II summarizes the fit parameters for the series. For all compositions, the model agrees well with the magnetization data measured along the easy axis, perpendicular to the film plane. The ratios of Heisenberg exchange constants are similar to those reported previously for an MRG film with a comparable composition [22]. The main trend that emerges from the data are that as the Ru content of MRG increases, $\mathcal{J}^{cc}$ decreases, while $\mathcal{J}^{aa}$ and $\mathcal{J}^{ac}$ remain almost constant. We explain the results as follows: $\mathcal{J}^{aa}$ does not depend on Ru content because Mn^{4a} does not have much overlap with Ru^{4d}. When the number of Mn atoms in the unit cell exceeds 16, some Mn fills the 4*d* positions, giving rise to Mn^{4c} - Mn^{4d} interactions, thereby the weakening $\mathcal{J}^{cc}$.

It is known that Mn-Mn distances in the range 250–280 pm generally lead to antiferromagnetic coupling that decreases in magnitude as the distance increases, whereas at distances greater than 290 pm, the coupling becomes ferromagnetic. [33] In an unstrained Mn_2RuGa film, $a_0 = 598$ pm. The intra-sublattice distances between Mn atoms, where each site forms

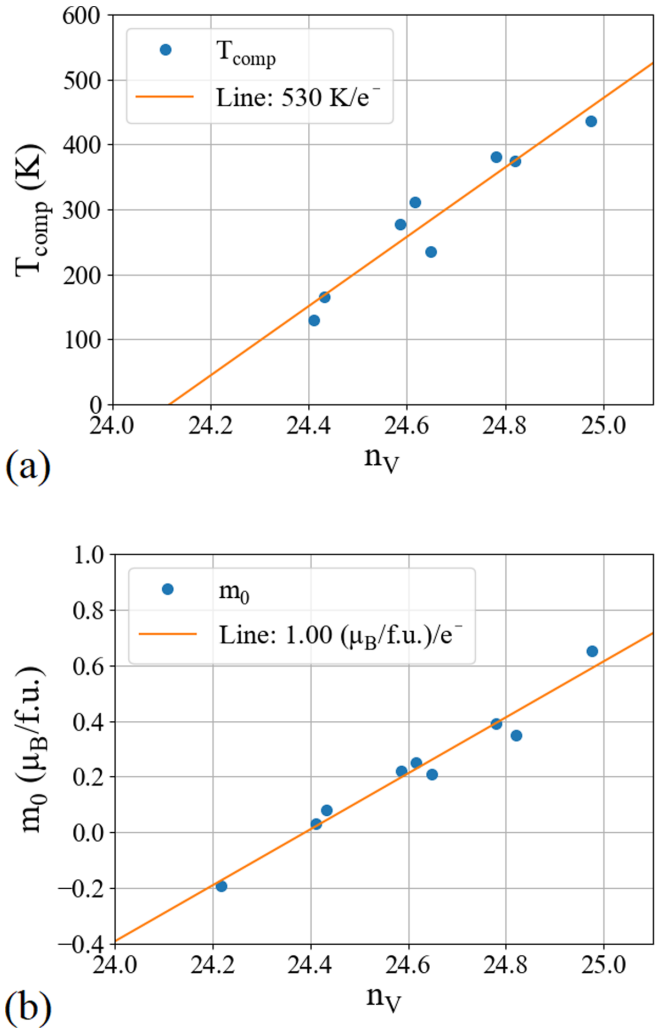

FIG. 10. (a) T_{comp} versus n_V: Adding an electron (e) raises T_{comp} by 530 K. (b) m_0 versus n_v: Adding an electron (e) raises m_0 by 1 μ_B/f.u. in agreement with the Slater-Pauling rule for a half-metal.

an fcc sublattice, are $a_0/\sqrt{2} \approx 423$ pm and the intersublattice Mn^{4a} - Mn^{4c} or Mn^{4b} - Mn^{4c} distance is $a_0\sqrt{3}/4 \approx 259$ pm, as indicated in Fig. 11. These distances correspond to ferromagnetic and antiferromagnetic exchange, respectively. They are changed a little by the tetragonal distortion. Since the densities indicate that all sites are occupied, chemical disorder will arise in the unit cell. A first type of disorder arises from Mn^{4a}-Ga^{4b} antisites and a second is the presence of Mn atoms on 4d sites. The Mn^{4c} sublattice portion of the unit cell is shown for Mn_2RuGa and $Mn_{2.25}Ru_{0.75}Ga$ in Figs. 11(a) and 11(b), respectively, where the latter illustrates both types of disorder. The presence of Mn on 4d sites gives rise to FM coupling, marked with green lines in Fig. 11(b). Changing the positions of Ga^{4b} and Mn^{4a} results in antiferromagnetic coupling because the Mn^{4b} - Mn^{4c} distance is ≈259 pm. This leads to random competing exchange on the Mn^{4c} sublattice, which will tend to produce a noncollinear spin structure. The local Mn^{4c} macroscopic sublattice moment may be expected to cant away from the anisotropy axis, forming an easy cone if fourfold in-plane anisotropy is negligible. The cone angle is the angle between the anisotropy axis and the moment.

TABLE II. Summary of sublattice magnetization at $T = 0$ K (M_0), spin angular momenta ($S^{4a,4c}$), and Heisenberg exchange parameters from molecular-field theory analysis of magnetization data on the nine MRG thin films. The last column shows the ratio of the product of exchange constants with the coordination number $\mathcal{J}^{aa}Z^{aa} : \mathcal{J}^{ac}Z^{ac} : \mathcal{J}^{cc}Z^{cc}$.

Mn, Ru	S^{4a}	S^{4c}	M_0^{4c}	$\mathcal{J}^{aa}$	$\mathcal{J}^{ac}$	$\mathcal{J}^{cc}$	Ratio
y, x			(kA/m)	(K)	(K)	(K)	
2.2, 0.5	2.0	2.0	431	22.0	−24.5	11.6	10.0 : −7.4 : 5.3
2.4, 0.5	2.5	2.5	471	19.7	−20.2	10.3	10.0 : −6.8 : 5.3
2.6, 0.5	2.5	2.5	503	19.4	−20.1	9.6	10.0 : −6.9 : 5.0
2.0, 0.7	2.0	2.5	478	21.6	−20.5	10.4	10.0 : −6.3 : 4.8
2.2, 0.7	2.0	2.5	508	21.7	−19.7	10.5	10.0 : −6.1 : 4.8
2.4, 0.7	2.0	2.5	532	19.2	−16.1	10.0	10.0 : −5.6 : 5.2
1.8, 0.9	1.5	2.5	501	21.8	−23.2	7.0	10.0 : −7.1 : 3.2
2.0, 0.9	1.5	2.5	526	23.0	−23.8	7.2	10.0 : −6.9 : 3.1
2.2, 0.9	1.5	2.5	576	22.4	−20.6	6.2	10.0 : −6.4 : 2.8

Local atomic environments differ on account of the random site occupancies that follow from the composition of the films, adding some randomness to the competing interactions and the local canting angle.

In-plane applied-field SQUID magnetometry data in Fig. 6 shows a component of the net moment that easily saturates along the *in-plane* field direction, unlike the hard component that normally extrapolates to the anisotropy field. For films with higher Ru content, which are closer to compensation at RT, the soft component dominates and the determination of the anisotropy field is problematic. From the data on the first two samples in Fig. 6, we deduce a cone angle for the net moment of 21°. A feature of the *out-of-plane* loops in Fig. 6, indicated by the purple arrow, is the step in magnetization near remanence that corresponds to 40% of the weak moment. We associate this with a closing of the Mn^{4c} cone and a simultaneous opening of a cone on the Mn^{4a} sublattice, for which we have seen evidence in XMCD data [32].

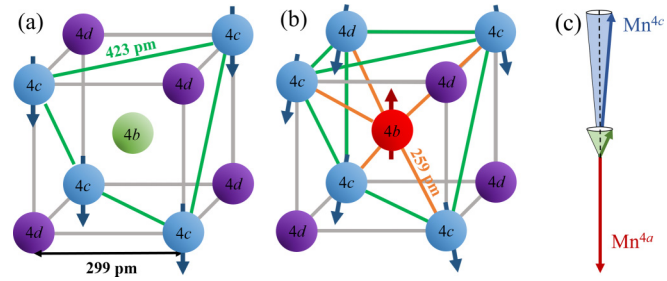

FIG. 11. Inner cube (Mn^{4c} sublattice) in the cubic unit cell of the inverse Heusler structure *XA* (Fig. 1) showing the (a) 4c and 4d sites occupied by Mn atoms (blue with arrow) and Ru atoms (purple) with Ga (green) in the center. (b) One Ru atom is replaced with an Mn atom on a 4d site and Ga is replaced with Mn on the 4b site (red with arrow). Nearest-neighbor ferromagnetic and antiferromagnetic couplings are represented by green and orange lines, respectively. The competition between exchange couplings can induce noncollinearity of sublattice moments locally. (c) Illustration of canting of net moment due to Mn^{4c} sublattice noncollinearity.

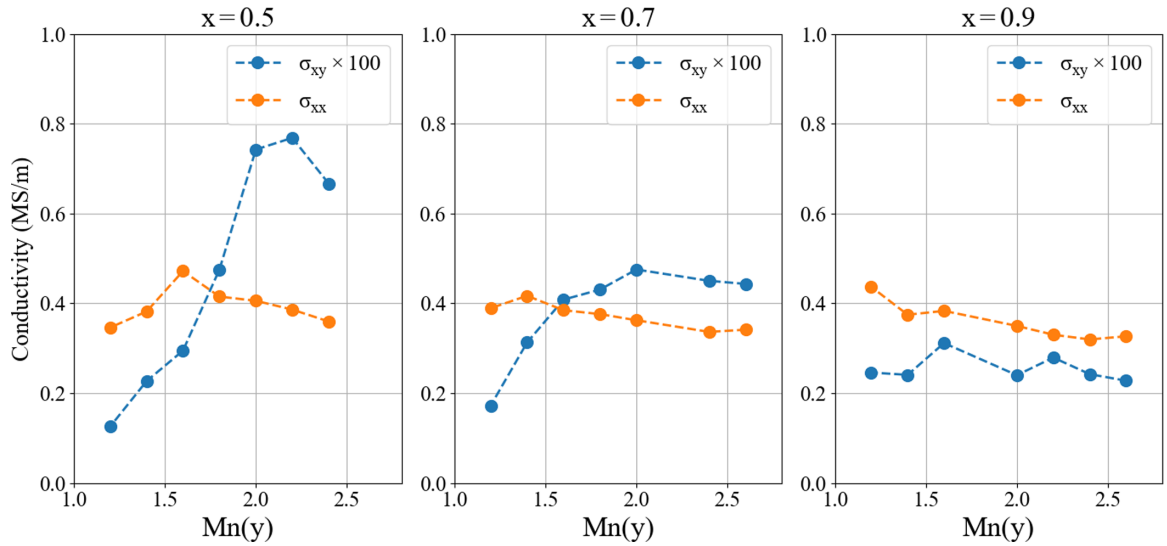

FIG. 12. Transverse (σ_{xy}) and longitudinal (σ_{xx}) conductivities of MRG thin films at 300 K for three Ru(x) series versus Mn(y) content. Note that σ_{xy} was calculated at magnetic saturation in $\mu_0 H = 1$ T at $T = 300$ K and the data in the graph have been multiplied by a factor of 100.

From the analysis of exchange energies and lattice parameters, it follows that sublattice noncollinearity results from competing positive and negative exchange coupling for the Mn^{4c} sublattice. This case has previously been argued for Mn^{2d} sites in tetragonal $D0_{22}$ Mn_2RhSn [34]. A picture that represents our experimental observations well appears on the right-hand side of Fig. 11(c). We note that the Mn^{4c} cone angle needs to be only a few degrees to result in canting of the net moment by tens of degrees, because the net moment is more than an order of magnitude smaller than the sublattice moments, depending on how close the temperature is to compensation. The AHE loops in Fig. 6, where R_{xy} is proportional to the perpendicular component of the Mn^{4c} sublattice magnetization, exhibit high remanence and we conclude that the very small in-plane moment of the Mn^{4c} sublattice cannot be detected.

The longitudinal (σ_{xx}) and transverse (σ_{xy}) conductivities of MRG thin films are plotted for three Ru(x) series versus Mn(y) in Fig. 12. The magnitude of σ_{xx} in the absence of a magnetic field is inversely proportional to the conduction electron scattering. In all samples, σ_{xx} is almost constant, whereas σ_{xy} shows a strong dependence on both Mn and Ru. To explain the observations, we need to consider the origins of AHE. There are two types of contributions to the anomalous conductivity. The first is the extrinsic contribution which is scattering dependent. Two distinct mechanisms are skew scattering and side jump, where the former is proportional to σ_{xx} and the latter is independent of σ_{xx}. The second, intrinsic contribution is scattering independent arising from Berry curvature and is independent of σ_{xx} [30].

In Fig. 12, σ_{xy} exhibits a decrease with increasing Ru content. When Mn is varied with low x, σ_{xy} is seen to be independent of σ_{xx}, but for $x = 0.9$, σ_{xy} is approximately constant. The independence of σ_{xy} on σ_{xx} and its strong dependence on Ru content x suggests that for low x films, the main contribution to AHE has an intrinsic origin. Impurity scattering, which depends on spin-orbit interaction, would be expected to increase with x. We find a maximal anomalous Hall angle $\theta_{AH} = 2\%$ for $Mn_{2.2}Ru_{0.5}Ga$, which is $\approx$10 times higher than in conventional ferromagnets measured at 300 K [35]. Such large Hall angles are consistent with a large intrinsic contribution. While this could be a Berry phase effect, we are unable to disentangle the possible contributions of band structure (Weyl points), noncollinearity, Fermi surface effects, and the influence of an incipient spin flop, which is expected for a ferrimagnet near compensation [36] and which is complete in $Mn_{2.2}Ru_{0.7}Ga$ at 7.65 T [32].

We finish the discussion comparing the $\approx 250 \mu\Omega$cm resistivity of $Mn_{2.2}Ru_{0.5}Ga$ with the $\approx 144 \mu\Omega$cm resistivity of pure αMn. There, the resistivity is substantially due to spin-disorder scattering and it varies by less than 10% between 50 K and RT [37]. The Néel temperature of αMn is 95 K. For MRG we observe an ordinary Hall coefficient of $\approx 0.02\Omega$/T, corresponding to a single-band carrier concentration $\approx 6 \times 10^{21}$cm^{-3}, which is an order of magnitude lower than for normal metals like Cu or Ru. The resulting mobility of 4 cm^2/Vs is comparable to that of Ru and substantially higher than that of αMn. Assuming a similar contribution of spin scattering, we find $(\frac{1}{2}\rho_{MRG})/\rho_{Mn} \approx 86\%$, where the factor $\frac{1}{2}$ for MRG is due to its half-metallic character. We conclude that the high resistivity of MRG is a direct consequence of the high ratio of spin-dependent scattering by hybrid states below E_F to momentum scattering, which is also the reason for the high spontaneous Hall angle, spin polarization, and intrinsic spin-orbit torque [17,20].

VI. CONCLUSIONS

At the outset, $Mn_2Ru_{0.5}Ga$ was assumed to have vacancies on the 4d sites. Here we have shown from the observed densities that all four sites in MRG are practically full, which implies that $Mn_2Ru_{0.5}Ga$ has 24 valence electrons, not 21 as originally thought. Full occupancy of the 4a and 4c sites

by Mn leads to a collinear ferrimagnetic structure, which accounts for the magnetic material properties.

The substantial absence of vacancies implies the presence of chemical disorder. Specifically, the presence of some Mn on 4*b* and 4*d* sites promotes antiferromagnetic intrasublattice exchange coupling on the Mn^{4c} sublattice, which leads to a noncollinear ferrimagnetic structure. The noncollinearity or the the small net moment is much more pronounced than that of the Mn^{4c} sublattice moment. The discrepancy between the AHE and the measurements of magnetization in Fig. 6 can therefore be explained. The independence of longitudinal and transverse conductivities indicates the dominance of the intrinsic contribution to AHE, which accounts for the large anomalous Hall angle observed in MRG films with low x. The reduction in spin polarization with increasing Ru corresponds to a narrowing of the spin gap in the density of states. The half-metallicity of MRG in the range of compositions investigated is confirmed by Slater-Pauling behavior of the net moment.

The magnetization, spin polarization, and compensation point of MRG can be tuned to match the requirements of a specific application by varying the composition of the films. Highly crystalline, textured thin films with magnetic compensation ranging from $T = 0\,\mathrm{K}$ up to the magnetic ordering temperature are produced. The coercivity near compensation that can exceed 10 T could permit the incorporation of single MRG layers in thin film stacks without any additional antiferromagnetic layers [24].

ACKNOWLEDGMENTS

K.E.S. and J.M.D.C. acknowledge funding through the Irish Research Council under Grant No. GOIPG/2016/308 and in part by the Science Foundation Ireland under Grants No. 12/RC/2278 and No. 16/IA/4534. G.A., A.J., R.S., S.L., J. O'B., P.S., and K.R. acknowledge funding from TRANSPIRE FET Open Programme, H2020. K.E. acknowledges funding from Science Foundation Ireland US-Ireland R&D (Center-to-Center) under Grant No. 16/USC2C/3287. N.T. was supported by the European Union's Horizon 2020 Research and Innovation Programme under Marie Skłodowska-Curie EDGE Grant No. 713567 and in part by the Science Foundation Ireland under Grant No. 16/IA/4534.

[1] D. Betto, K. Rode, N. Thiyagarajah, Y.-C. Lau, K. Borisov, G. Atcheson, M. Žic, T. Archer, P. Stamenov, and J. M. D. Coey, The zero-moment half metal: How could it change spin electronics? AIP Adv. **6**, 055601 (2016).

[2] J. Finley and L. Liu, Spintronics with compensated ferrimagnets, Appl. Phys. Lett. **116**, 110501 (2020).

[3] T. Graf, C. Felser, and S. S. Parkin, Simple rules for the understanding of Heusler compounds, Prog. Solid State Chem. **39**, 1 (2011).

[4] H. van Leuken and R. A. de Groot, Half-Metallic Antiferromagnets, Phys. Rev. Lett. **74**, 1171 (1995).

[5] S. Wurmehl, H. C. Kandpal, G. H. Fecher, and C. Felser, Valence electron rules for prediction of half-metallic compensated-ferrimagnetic behaviour of Heusler compounds with complete spin polarization, J. Phys.: Condens. Matter **18**, 6171 (2006).

[6] X. Hu, Half-metallic antiferromagnet as a prospective material for spintronics, Adv. Mater. **24**, 294 (2012).

[7] I. Galanakis, P. Mavropoulos, and P. Dederichs, Electronic structure and Slater–Pauling behaviour in half-metallic Heusler alloys calculated from first principles, J. Phys. D **39**, 765 (2006).

[8] P. Kharel, Y. Huh, N. Al-Aqtash, V. R. Shah, R. F. Sabirianov, R. Skomski, and D. J. Sellmyer, Structural and magnetic transitions in cubic Mn_3Ga, J. Phys.: Condens. Matter **26**, 126001 (2014).

[9] M. Hakimi, M. Venkatesan, K. Rode, K. Ackland, and J. M. D. Coey, The zero-magnetization Heusler ferrimagnet, J. Appl. Phys. **113**, 17B101 (2013).

[10] H. Kurt, K. Rode, P. Stamenov, M. Venkatesan, Y.-C. Lau, E. Fonda, and J. M. D. Coey, Cubic Mn_2 Ga Thin Films: Crossing the Spin Gap with Ruthenium, Phys. Rev. Lett. **112**, 027201 (2014).

[11] M. E. Jamer, Y. J. Wang, G. M. Stephen, I. J. McDonald, A. J. Grutter, G. E. Sterbinsky, D. A. Arena, J. A. Borchers, B. J. Kirby, L. H. Lewis, B. Barbiellini, A. Bansil, and D. Heiman, Compensated Ferrimagnetism in the Zero-Moment Heusler Alloy Mn_3Al, Phys. Rev. Appl. **7**, 064036 (2017).

[12] R. Stinshoff, G. H. Fecher, S. Chadov, A. K. Nayak, B. Balke, S. Ouardi, T. Nakamura, and C. Felser, Half-metallic compensated ferrimagnetism with a tunable compensation point over a wide temperature range in the Mn-Fe-V-Al Heusler system, AIP Adv. **7**, 105009 (2017).

[13] N. Thiyagarajah, Y.-C. Lau, D. Betto, K. Borisov, J. M. D. Coey, P. Stamenov, and K. Rode, Giant spontaneous Hall effect in zero-moment Mn_2Ru_xGa, Appl. Phys. Lett. **106**, 122402 (2015).

[14] K. E. Siewierska, N. Teichert, R. Schäfer, and J. M. D. Coey, Imaging domains in a zero-moment half metal, IEEE Trans. Magn. **55**, 1 (2019).

[15] N. Teichert, G. Atcheson, K. Siewierska, M. N. Sanz-Ortiz, M. Venkatesan, K. Rode, S. Felton, P. Stamenov, and J. M. D. Coey, Magnetic reversal and pinning in a perpendicular zero-moment half-metal, Phys. Rev. Materials **5**, 034408 (2021).

[16] G. Bonfiglio, K. Rode, K. Siewerska, J. Besbas, G. Y. P. Atcheson, P. Stamenov, J. M. D. Coey, A. V. Kimel, T. Rasing, and A. Kirilyuk, Magnetization dynamics of the compensated ferrimagnet Mn_2Ru_xGa, Phys. Rev. B **100**, 104438 (2019).

[17] S. Lenne, Y.-C. Lau, A. Jha, G. Y. P. Atcheson, R. E. Troncoso, A. Brataas, J. M. D. Coey, P. Stamenov, and K. Rode, Giant spin-orbit torque in a single ferrimagnetic metal layer, arXiv:1903.04432 (2019).

[18] M. Cubukcu, O. Boulle, M. Drouard, K. Garello, C. Onur Avci, I. Mihai Miron, J. Langer, B. Ocker, P. Gambardella, and G. Gaudin, Spin-orbit torque magnetization switching of a three-terminal perpendicular magnetic tunnel junction, Appl. Phys. Lett. **104**, 042406 (2014).

[19] L. Liu, O. J. Lee, T. J. Gudmundsen, D. C. Ralph, and R. A. Buhrman, Current-Induced Switching of Perpendicularly Magnetized Magnetic Layers Using Spin Torque from the Spin Hall Effect, Phys. Rev. Lett. **109**, 096602 (2012).

[20] J. Finley, C.-H. Lee, P. Y. Huang, and L. Liu, Spin–orbit torque switching in a nearly compensated Heusler ferrimagnet, Adv. Mater. **31**, 1805361 (2019).

[21] C. Banerjee, N. Teichert, K. Siewierska, Z. Gercsi, G. Atcheson, P. Stamenov, K. Rode, J. M. D. Coey, and J. Besbas, Single pulse all-optical toggle switching of magnetization without gadolinium in the ferrimagnet Mn_2Ru_xGa, Nat. Commun. **11**, 4444 (2020).

[22] C. S. Davies, G. Bonfiglio, K. Rode, J. Besbas, C. Banerjee, P. Stamenov, J. M. D. Coey, A. V. Kimel, and A. Kirilyuk, Exchange-driven all-optical magnetic switching in compensated 3*d* ferrimagnets, Phys. Rev. Research **2**, 032044(R) (2020).

[23] C. Banerjee, K. Rode, G. Atcheson, S. Lenne, P. Stamenov, J. M. D. Coey, and J. Besbas, Ultrafast Double Pulse All-Optical Reswitching of a Ferrimagnet, Phys. Rev. Lett. **126**, 177202 (2021).

[24] K. Borisov, D. Betto, Y. C. Lau, C. Fowley, A. Titova, N. Thiyagarajah, G. Atcheson, J. Lindner, A. M. Deac, J. M. D. Coey, P. Stamenov, and K. Rode, Tunnelling magnetoresistance of the half-metallic compensated ferrimagnet Mn_2Ru_xGa, Appl. Phys. Lett. **108**, 192407 (2016).

[25] M. Žic, K. Rode, N. Thiyagarajah, Y.-C. Lau, D. Betto, J. M. D. Coey, S. Sanvito, K. J. O'Shea, C. A. Ferguson, D. A. MacLaren, and T. Archer, Designing a fully compensated half-metallic ferrimagnet, Phys. Rev. B **93**, 140202(R) (2016).

[26] D. Betto, N. Thiyagarajah, Y.-C. Lau, C. Piamonteze, M.-A. Arrio, P. Stamenov, J. M. D. Coey, and K. Rode, Site-specific magnetism of half-metallic Mn_2Ru_x Ga thin films determined by x-ray absorption spectroscopy, Phys. Rev. B **91**, 094410 (2015).

[27] I. V. Soldatov and R. Schäfer, Advanced MOKE magnetometry in wide-field kerr-microscopy, J. Appl. Phys. **122**, 153906 (2017).

[28] P. Stamenov, Point contact Andreev reflection from semimetallic bismuth - the roles of the minority carriers and the large spin-orbit coupling, J. Appl. Phys. **113**, 17C718 (2013).

[29] K. Borisov, C.-Z. Chang, J. S. Moodera, and P. Stamenov, High Fermi-level spin polarization in the $(Bi_{1-x}Sb_x)_2Te_3$ family of topological insulators: A point contact Andreev reflection study, Phys. Rev. B **94**, 094415 (2016).

[30] N. Nagaosa, J. Sinova, S. Onoda, A. H. MacDonald, and N. P. Ong, Anomalous Hall effect, Rev. Mod. Phys. **82**, 1539 (2010).

[31] J. Smart, *Effective Field Theories of Magnetism* (Saunders, London, 1966).

[32] K. Siewierska, D. Betto, N. Teichert, G. Atcheson, N. Brookes, and K. Rode, XMCD investigation of sublattice non-collinearity in compensated ferrimagnetic half-metallic thin films, 2021 (unpublished).

[33] J. M. D. Coey, Magnetic materials, *Magnetism and Magnetic Materials* (Cambridge University Press, Cambridge, 2010), pp. 395–396.

[34] O. Meshcheriakova, S. Chadov, A. K. Nayak, U. K. Rößler, J. Kübler, G. André, A. A. Tsirlin, J. Kiss, S. Hausdorf, A. Kalache, W. Schnelle, M. Nicklas, and C. Felser, Large Noncollinearity and Spin Reorientation in the Novel Mn_2RhSn Heusler Magnet, Phys. Rev. Lett. **113**, 087203 (2014).

[35] T. Seki, S. Iihama, T. Taniguchi, and K. Takanashi, Large spin anomalous Hall effect in $L1_0-FePt$: Symmetry and magnetization switching, Phys. Rev. B **100**, 144427 (2019).

[36] T. Fu, S. Li, X. Feng, Y. Cui, J. Yao, B. Wang, J. Cao, Z. Shi, D. Xue, and X. Fan, Complex anomalous Hall effect of CoGd alloy near the magnetization compensation temperature, Phys. Rev. B **103**, 064432 (2021).

[37] F. Boakye, K. Adanu, and A. Grassie, Critical scattering of conduction electrons around the néel temperature of α-manganese thin films, Mater. Lett. **18**, 320 (1994).